Journal of Alloys and Compounds 712 (2017) 320–333

Contents lists available at ScienceDirect

Journal of Alloys and Compounds

journal homepage: http://www.elsevier.com/locate/jalcom

Correlation between structural, magnetic and ferroelectric properties of Fe-doped (Ba-Ca)TiO_3 lead-free piezoelectric

B.C. Keswani [a], R.S. Devan [b], R.C. Kambale [a], A.R. James [c], S. Manandhar [d], Y.D. Kolekar [a, **], C.V. Ramana [d, *]

[a] Department of Physics, Savitribai Phule Pune University, Pune 411007, Maharashtra, India
[b] Centre for Physical Sciences, School of Basic and Applied Sciences, Central University of Punjab, Bathinda 151001, India
[c] Defence Metallurgical Research Laboratory, Hyderabad 500058, India
[d] Department of Mechanical Engineering, University of Texas at El Paso, El Paso, TX 79968, USA

ARTICLE INFO

Article history:
Received 3 January 2017
Received in revised form
21 February 2017
Accepted 25 March 2017
Available online 27 March 2017

Keywords:
$(Ba,Ca)TiO_3$
Fe-doping
Multiferroics
Crystal structure
Ferroelectric properties

ABSTRACT

The effect of iron (Fe) doping modification on the structure and properties of $Ba_{0.92}Ca_{0.08}TiO_3$ (BCT8) lead-free ferroelectrics is investigated in detail. Intrinsic $BaTiO_3$ (BT) and $Ba_{0.92}Ca_{0.08}TiO_3$ (BCT8) lead-free polycrystalline ceramics were synthesized by conventional solid-state chemical reaction method. The crystal structure, morphology, chemical composition and valence state, magnetic and ferroelectric properties of BCT8 ceramics were evaluated as a function of variable Fe-content (0–5 wt%). X-ray diffraction measurements coupled with Rietveld refinement analyses indicate that the BT, BCT8, and Fe-BCT8 ceramics crystallize in single phase tetragonal structure. Phase transformation occurs with higher Fe doping; Fe-BCT8 ceramics with 5 wt% Fe exhibits fully transformed orthorhombic structure. The crystal structure and phase formation of these ceramics was further confirmed by the Raman spectroscopic (RS) measurements. The RS data coupled with high-resolution X-ray photoelectron spectroscopic (XPS) analyses also confirm the formation of single phase materials without any presence of secondary or impurity phases. Microstructure imaging analyses indicate that the grain size was ~1 μm, while agglomeration and inhomogeneous distribution were observed with Fe doping. Polarization-electric field (P-E) hysteresis and strain-electric field (S-E) hysteresis measurements revealed the ferroelectric and piezoelectric nature of the ceramics. Ferroelectric and piezoelectric properties were observed to be suppressed for Fe doped BCT8 ceramics due to the partial replacement of Ti^{4+} by Fe^{3+} as confirmed by the chemical analyses made using XPS. Temperature dependent dielectric measurements for Fe doped BCT8 show a drastic decrease in ferroelectric Curie temperature (T_c), along with a decrease in dielectric constant compared to that of undoped BCT8. Magnetization (M-H) measurements confirm the presence of long-range magnetic ordering for 5% Fe-doped BCT8 sample. The results demonstrate that addition of 5% Fe in lead-free BCT8 perovskite induces the magnetic ordering and a switchable ferroelectric state, which evidences the presence of multiferroic nature that can be used for four-bit memory and switching applications.

1. Introduction

Multifunctional materials, which can combine multiple properties and phenomena in the solid state, are increasingly gaining recent attention by the scientific and research community. In addition to finding numerous technological applications, such materials offer an approach to design a novel, single solid state material with many different properties so as to achieve *rich functionality* [1–3]. Recently, strong attention has been paid toward multiferroics, which can exhibit simultaneously ferroelectricity and magnetic order, due to their potential applications in current and emerging technologies [1–6]. Multiferroics feature the characteristic property that the magnetic and dielectric order parameters are coupled, so that the ferroelectricity can be controlled by magnetism and vice versa [1–5].

* Corresponding author.
** Corresponding author.
E-mail addresses: ydkolekar@gmail.com (Y.D. Kolekar), rvchintalapalle@utep.edu (C.V. Ramana).

http://dx.doi.org/10.1016/j.jallcom.2017.03.301
0925-8388/

The piezoelectric materials along with subclasses of ferroelectrics and pyroelectrics are particularly attractive for a number of applications in electronics, micromechanics, sensors, actuators, magneto-electronics and energy harvesting applications [1,2,7–10]. Especially, the piezoelectric and ferroelectric properties, which often exists in the same material, provide excellent means to harvest energy from multiple sources, which include mechanical, electrical, vibration and optical [10,11]. Piezoelectric materials are commonly employed in sensor and actuator technologies due to their unique ability to couple electrical and mechanical displacements, *i.e.,* to change electrical polarization in response to an applied mechanical stress or mechanically strain in response to an applied electric field [7,10]. The lead (Pb) based materials, such as $Pb(Zr,Ti)O_3$ abbreviated as PZT, are the most commonly used piezoelectric materials. The PZT materials are widely used in a variety of technological applications, such as actuators, sensors, ultrasound transducers, high dielectric capacitors, and ferroelectric thin film memories [8,10]. The dominance of PZT-based in the technological applications and development is mostly due to their superior properties, such as high Curie temperature ($T_c \approx 390\ ^\circ C$), high dielectric constant (ε~20000 at T_c), low dielectric loss ($\tan\delta \sim 0.004$), and high piezoelectric coefficient ($d_{33} \sim 220$ pC/N) [12,13]. However, the critical disadvantage of PZT is that it contains more than 60 wt% of Pb. The large amount of toxic Pb-content creates health and environmental hazards. Therefore, for global environment protection, scientific and research community across the globe have directed efforts on the discovery, design, and development of Pb-free ferroelectrics and piezoelectrics, which can exhibit similar or comparable or even superior properties to that of PZT.

The perovskite structured barium titanate ($BaTiO_3$, which abbreviated BT hereafter), which is a classical ferroelectric, and BT-based solid solutions are an important class of materials that show a large piezoelectric response and a high dielectric constant useful for all of the aforementioned technological applications [3,14–17]. In fact, among the known Pb-free materials such as $(K_{1-x}Na_x)NbO_3$ (KNN), $(Bi_{1-x}Na_x)TiO_3$ (BNT), $BaTiO_3$, BT-based materials are of great practical interest due to their excellent properties such as relatively high stability, high dielectric constant (ε'~1700), low dielectric loss ($\tan\delta$~0.01), and moderately high piezoelectric coefficient ($d_{33} \sim$ 150 pC/N). Recently, $BaTiO_3$ based hetero-structures were also demonstrated for efficient use in solar cells and have been the subject of utilization for energy related applications [6]. Moreover, its stable chemical stoichiometry, after sintering, makes it one of the important ferroelectric materials for applications in piezoelectric sonar, ultrasonic transducer, high dielectric capacitor, multilayer capacitors (MLCs), sensors, switches, and ferroelectric thin film memories, etc. However, the Curie temperature ($T_c \sim 120\ ^\circ C$) resulted in narrower working temperature range and hindered its practical piezoelectric applications [18,19]. The partial substitution of Ca^{2+} at Ba^{2+} site in $BaTiO_3$ can help to increase the temperature range stability of the tetragonal phase [20–22]. Additionally, it has been widely recognized that Ca doping plays a key role in achieving tunable electrical and dielectric properties of $BaTiO_3$.

Currently, there is a great demand for materials which possesses the simultaneous ferroelectric and magnetic ordering, the so-called multiferroic materials. Among the known single phase multiferroic materials, $BiFeO_3$ is the single phase multiferroic at room temperature but it suffers from weak magnetization, and low density, which limits its integration into practical applications [23,24]. Introducing or doping the transition metal (TM) ions in the perovskite oxides can induce magnetic ordering and helps to overcome some of these limitations [6]. To this end, several attempts were made by several research groups to induce magnetism in $BaTiO_3$ using suitable magnetic ions. It has been reported that Cr, Mn, Fe and Ni are the most suitable TM ions to effectively induce magnetism in $BaTiO_3$ [2,25–30]. Recently, significant efforts were directed to the Fe-doped BT system, where the focus was towards understanding the structural, ferroelectric and magnetic properties of both bulk and thin films [26,30–36]. For instance, Maikhuri et al. have investigated the ferroelectric and magnetic properties of 10 at % Fe substitution at both Ba- and Ti- site, respectively, in $BaTiO_3$ and revealed the multiferroic nature in both the cases [36]. However, while TM-content was arbitrarily chosen in most of the cases, the efforts to understand a correlation between variable TM-ion content, crystal chemistry, microstructure, ferroelectric, magnetic, piezoelectric and dielectric properties are meager. Furthermore, although there are some reports available on the ferroelectric and magnetic properties of transition metal ion doped $BaTiO_3$, no detailed investigation is available on the structural, ferroelectric, piezoelectric and magnetic properties of Fe-doped Ca-modified $Ba_{0.92}Ca_{0.08}TiO_3$ (BCT8) ceramics. Therefore, the present work was directed to derive a fundamental understanding of the effect of Fe doping on the structural, morphology, dielectric, ferroelectric, piezoelectric and magnetic properties of the BCT8 system. The objective is to realize highly dense materials so that the ferroelectric and magnetic ordering would be present in a single phase. Furthermore, since it is well known that Ca-doped (at Ba) site in $BaTiO_3$ can allow tunable electrical characteristics, Fe-doping into BCT so as to induce magnetism and finding an optimum configuration could provide fundamental, efficient means to tailor the materials' properties and phenomena, which can be readily utilized in many of the aforementioned technological applications. Thus, the efforts were directed to derive a correlation between crystal chemistry, chemical composition, chemical valence state, microstructure, ferroelectric, piezoelectric, magnetic and dielectric properties in Fe-doped BCT8 ceramics. The results presented and discussed in this paper demonstrate that addition of 5% Fe in lead-free BCT8 perovskite induces the magnetic ordering and a switchable ferroelectric state, which evidences the presence of multiferroic nature that can be used for four-bit memory and switching device applications.

2. Experimental details

2.1. Synthesis

All the ceramics with variable composition, viz., $BaTiO_3$ (BT), $Ba_{0.92}Ca_{0.08}TiO_3$ (BCT8) and Fe-doped (0–5 wt %) BCT8, were synthesized by standard solid state chemical reaction method using high purity (>99%) $BaCO_3$, TiO_2, $CaCO_3$, Fe_2O_3 precursors (all are from Sigma-Aldrich). All the precursors were weighed with their stoichiometric proportions and ball milled in an ethanol medium with the help of zirconium balls followed by grinding in an agate mortar. The powders were then calcinated at 1050 °C for 5 h in an ambient atmosphere. After calcination, the powders were grounded, pressed into pellets (diameter ~10 mm and thickness ~ 1 mm) using a hydraulic press for different characterizations. The Polyvinyl alcohol (PVA) was used as a binder to make the pellets with good density and all the pellets were finally sintered at 1240 °C for 5 h in an ambient atmosphere with the heating rate of 2°/min and cooled to 300 °C with 2°/min then followed by natural cooling to room temperature. All the pellets obtained at 1240 °C were found to be dense except BT and therefore, BT was further sintered at 1300 °C for 5 h with the same rate of heating and cooling.

2.2. Characterization

The phase formation and structural analyses were made using X-ray diffraction (XRD) measurements. The XRD measurements

were made using a Bruker D8 Advance X-ray diffractometer (XRD) (Cu k_α having $\lambda = 1.5406$ Å). The phase formation of all the synthesized samples was confirmed from XRD patterns. To derive a more detailed account of structural properties, Rietveld refinements were also performed employing Fullprof software. For Rietveld refinement, shape of Bragg peaks was modified by pseudo-Voigt function, which is a combination of Gaussian and Lorentzian function. The background of XRD pattern was fitted with the linear interpolation between a set background points and refinable heights. During the fitting process, scale factors, cell parameters, shape parameters, FWHM parameters, and zero angular shifts were refined. The morphology of the BT, BCT, and Fe-doped BCT ceramics was studied by using a field emission scanning electron microscope (FESEM JEOL JSM- 6500F). X-ray photoelectron spectroscopy (XPS) measurements were carried out using a spectrometer (XPS Thermoscientific Inc K-alpha) with microfocus Al-K_α monochromatic X-rays ($h\nu = 1486.6$ eV). The survey scans as well as core-level XPS spectra were recorded in order to understand the chemical valence state of cations in these ceramics. XPS data were used to determine the oxidation state and chemical environment of cations. All the XPS spectra were deconvoluted via Voigt curve fitting function with Shirley background subtraction.

Raman spectra were recorded using a micro-Raman system (Reinshaw) with 532 nm laser excitation. Electroding of samples was done using silver paste on both the sides of mirror polished pellets and heated at 100 °C for 4 h to cure the silver paste. The electroded samples were then used for dielectric measurements using HIOKI 3532-50 LCR HiTESTER, polarization versus electric field (P-E) hysteresis loops and field-induced strain (S-E) hysteresis loop measurements using a ferroelectric test system (aixAcct systems, GMBH TF ANALYSER 2000. TREk model 610 E). Magnetic measurements were performed at temperatures 10 K, 100 K and 300 K using a Vibrating Sample Magnetometer (VSM Lakeshore 7407).

3. Results and discussion

XRD patterns of all the ceramics along with Rietveld refinement data of all the ceramics are shown in Fig. 1. XRD patterns of BT, BCT8 and 1.25% Fe-doped BCT8 samples were refined to *P4mm* space group with tetragonal structure and all the observed peaks were matched with the ICSD (Inorganic Crystal Structure Database) collection code 161340 and indexed accordingly. While 5% Fe-doped BCT8 samples were refined to *Amm2* space group with the orthorhombic structure. All the observed peaks were matched with ICSD collection code 31155 and indexed accordingly. The Rietveld fitted XRD patterns of all the synthesized samples are as shown in Fig. 1, where the composition of the ceramic is clearly indicated. The lattice parameters, X-ray density, χ^2 values, R_f factor, the goodness of fit factor (GofF) and Bragg R-factor are presented in Table 1. The

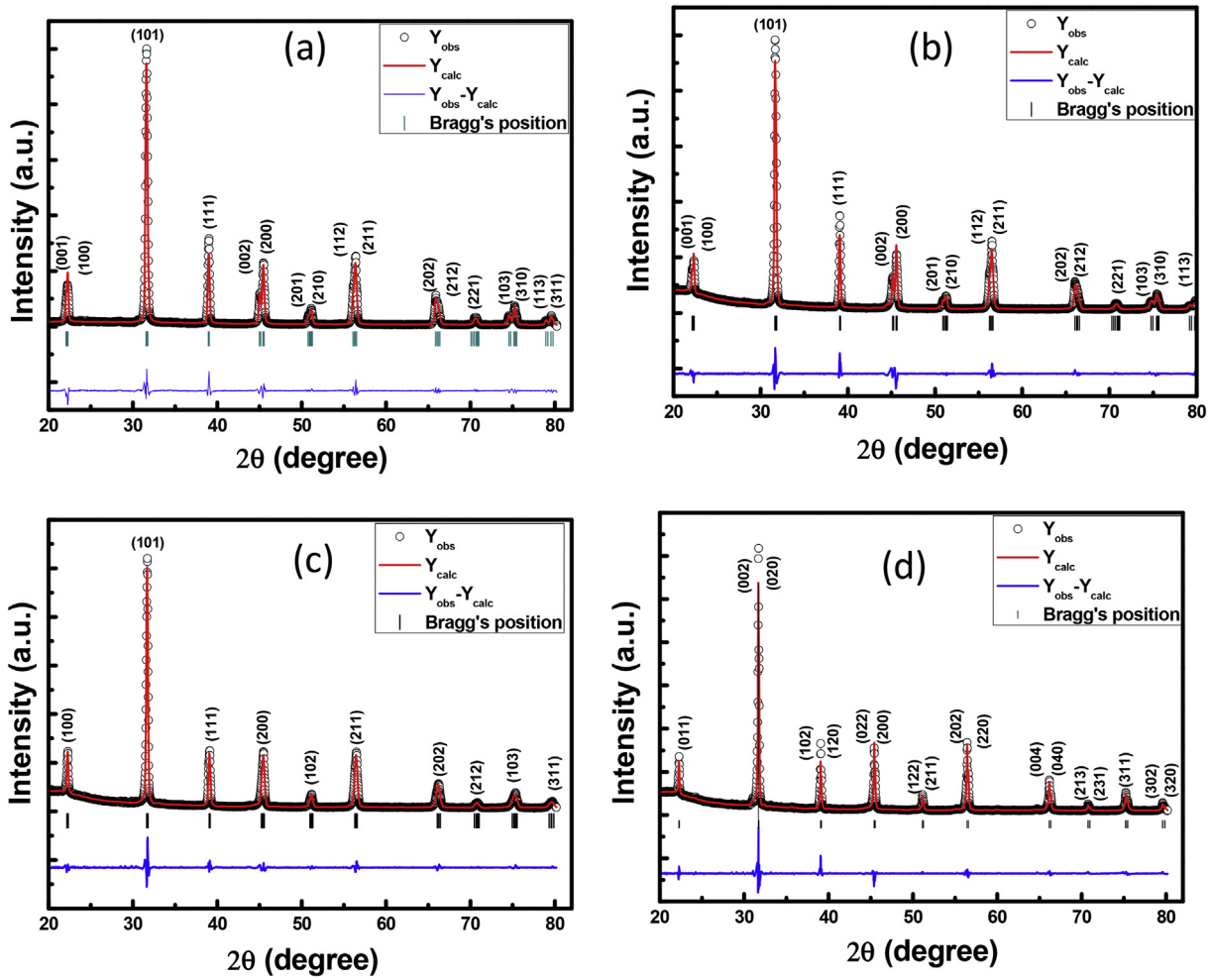

Fig. 1. XRD data of BT, BCT8 and Fe doped BCT8 ceramics. The experimental XRD patterns along with fitting with Reitveld refinement are shown. Rietveld fitted XRD patterns shown are: (a) BT, (b) BCT8, (c) Fe(1.25%) doped BCT8, and (d) Fe(5%) doped BCT8.

Table 1
The values of lattice parameter, *c/a* ratio, unit cell volume (*V*), crystallite size (*t*), grain size, x-ray density (ρ), chi square (χ^2), R_f factor, Goodness of fit factor (*GofF*), Bragg R factor values for BT, BCT8 and Fe doped BCT8 samples.

Composition	*a* (Å)	*c*(Å)	*c/a*	*V* (Å)^3	*t* (nm)	Grain size (μm)	ρ (g/cm^3)	χ^2	R_f factor	GofF ($\frac{R_{wp}}{R_{exp}}$)	Bragg *R* factor
BT	3.9901	4.0253	1.0088	64.0858	39	0.5	6.041	2.29	1.76	1.5	3.49
BCT8	3.9808	4.0154	1.0087	63.6302	59	0.8	5.8816	9.11	2.14	3	4.25
BCT8:1.25% Fe	3.9875	4.0056	1.0045	63.6909	44	0.25	5.9280	6.62	0.75	2.5	1.71
BCT8:5% Fe	***a* (Å)**	***b* (Å)**	***c* (Å)**	127.1565	74	agglomeration	6.0949	8.99	2.78	3	3.91
	3.9895	5.6449	5.6463								

lower values of χ^2 and GofF indicate the good agreement between the calculated and observed patterns. The crystallite size (t) was calculated by using Scherrer formula,

$$t = \frac{0.9\,\lambda}{\beta \cos\theta_B} \quad (1)$$

where, λ is the wavelength of Cu (K_α) = 1.5406 Å, β is full width at half maxima (FWHM), θ_B Bragg's angle.

The high-resolution XRD peak observed at 2θ ~45° is shown separately in Fig. 2, where the splitting of (002) and (200) peaks is evident. This observation confirms the stable tetragonal structure in BT, BCT8 and Fe-doped BCT ceramics. However, for increasing Fe content, BCT8 sample with 1.25 wt% Fe shows indistinct splitting of (002) and (200) peaks as noted in Fig. 2(c) The splitting of (002) and (200) is due to the electrostatic repulsion between 3d electrons of Ti^{4+} ions and 2p electrons of O^{2-} ions [28]. The indistinct splitting of (002) and (200) peaks observed may be an indication of the fact that higher Fe content in BCT may induce a slight deviation of the structure from the stable tetragonal structure. It is important to recognize that, in the case of 5% Fe-doped BCT8 sample, all the observed peaks except (011) at 2θ~22° show (Fig. 2(d)) a significant splitting, which is a characteristic feature of the orthorhombic structure. The magnified view of (022) and (200) peak splitting, which is shown in Fig. 2(d), indicates the characteristic orthorhombic structure. The lattice parameters obtained for BT, BCT8 and

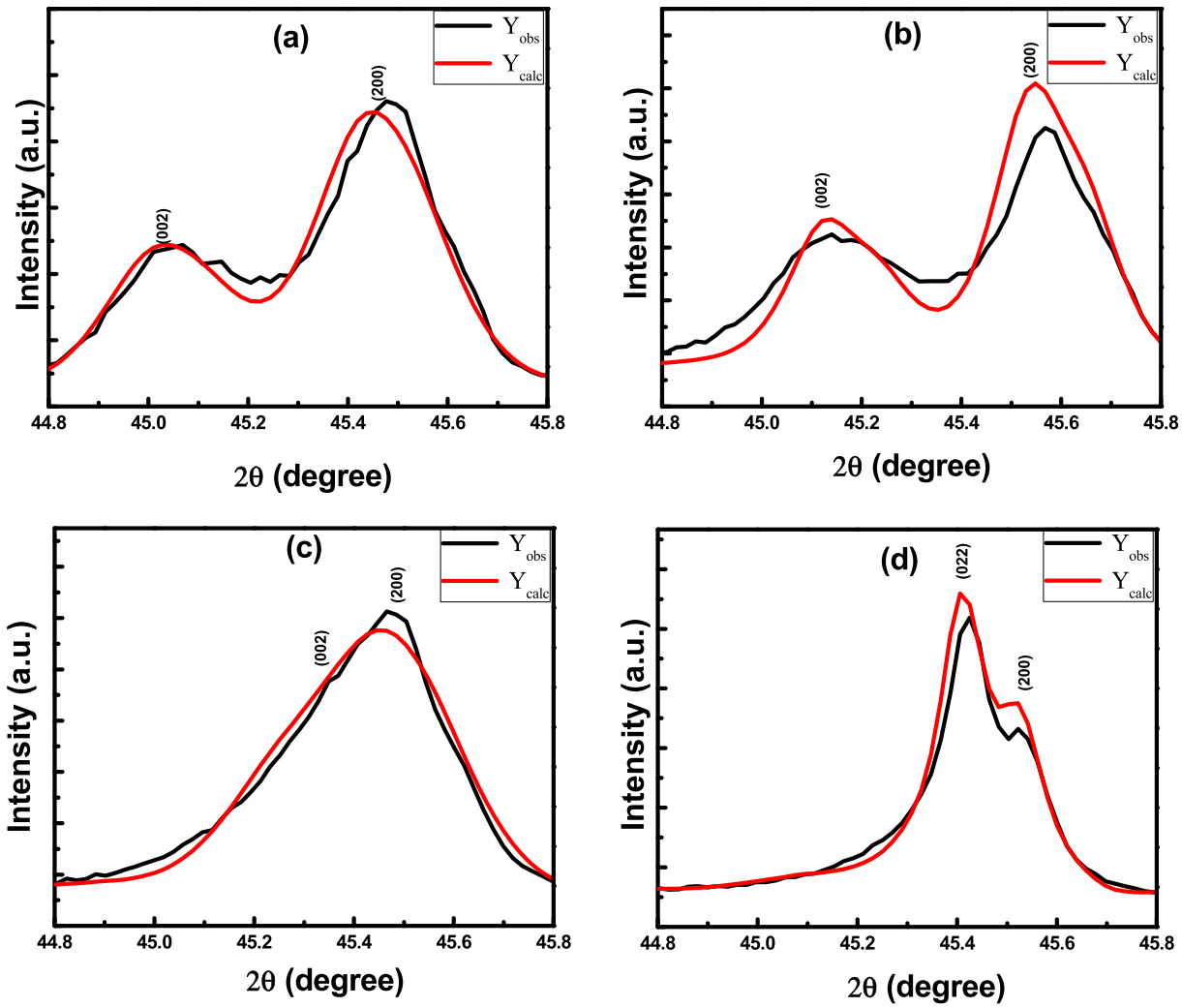

Fig. 2. Splitting of (002) and (200) XRD peak. The data shown are: (a) BT, (b) BCT8, (c) Fe(1.25%) doped BCT8, and (d) Fe(5%) doped BCT8. The changes in peak splitting as a function of Fe content are evident.

their *c/a* ratio are comparable with the reported data [37]. The lattice parameter values for BCT8 observed to be decreasing compared to BT due to the substitution of Ba^{2+} (1.61 Å) by smaller Ca^{2+} ion (1.34 Å). Also, with Fe doping, the lattice parameter '*c*' decreases as noted for 1.25% Fe in BCT8. This characteristic feature is the signature of the fact that the Fe doping into BCT system is resulting in the distortion leading to structural perturbation which deviates the structure from the stable tetragonal structure. The phase transformation becomes fully complete as seen with increasing Fe content. For 5% Fe-doped BCT8, there is a complete phase transformation from tetragonal to the orthorhombic structure as is evident in XRD studies. The crystallite size calculated was in the range of 39–80 nm. The X-ray density was observed to be decreasing with Ca substitution due to the increase in grain size as observed from FE-SEM images (Fig. 3). For 5% Fe-doped BCT8, X-ray density increases due to a further decrease in grain size and agglomeration. The bond length between different ions in the unit cell was also calculated from Rietveld refinement. The calculated values of bond length between Ti–O, Ba–O, Ba–Ti, Ba–Ba and the number of these bonds present in the unit cell are tabulated in Table 2. From the values of bond length between different ions, it is observed that the bond lengths of Ti–O bonds remain almost same for BCT8 as that of BT. This observation illustrates that the tetragonal structure remains stable even after Ca substitution. On the other hand, the significant change in bond length values observed for Fe doped BCT sample accounts for the observed structural deviation from the tetragonal structure. Due to off-centering of Ti^{4+}, there are four long and four short Ba–Ti distances in the unit cell of tetragonal BT. From Ba–Ti distances, the distortion parameter for tetragonal BT is calculated [26]. It is observed that the calculated distortion parameter is 0.0121, which remains same for BT and BCT8 samples. However, this value further decreases to 0.0120 for 1.25% Fe-doped samples. Thus, from structural characterization, it is evident that the tetragonal structure remains stable even with Ca substitution. The structural distortion occurs with Fe doping. Also, among all the studied samples, Ti–O, Ba–O and Ba–Ti bonds of BCT8 are strained while in the case of Fe-doped BCT8 these bonds are relaxed [21].

FESEM images of BT, BCT8 and Fe-doped BCT8 samples are shown in Fig. 3. BT and BCT8 show clearly visible grains with average grain size in the range of 0.5–1 μm, while Fe-doped BCT8 shows agglomeration with variable size clusters i.e., becomes inhomogeneous distribution with Fe doping. The non-uniform microstructure of 5% Fe-doped BCT8 is the indication of faster nucleation than the grain growth [28], which might have occurred due to oxygen vacancies created after replacing Ti^{4+} ions with Fe^{3+} ions to further decrease the mobility of ions resulting in slower lower grain growth [38]. Furthermore, an increase in agglomeration and decrease in the porosity is observed with increase in Fe concentration which may be due to the highly reactive nature of Fe ions. Consequently, the density of samples increase with Fe doping and is in good agreement with the calculated X-ray density. This signifies that the incorporation of trivalent transition metal ion impurity such as Fe^{3+} in the perovskite lattice of BCT8 leads to alter the microstructure of the BCT8.

The oxidation state and chemical environment of the synthesized samples were analyzed using XPS. Fig. 4 presents the high-resolution XPS spectra for the Ba 3*d*, Ca 2*p*, Ti 2*p*, and O 1*s* core

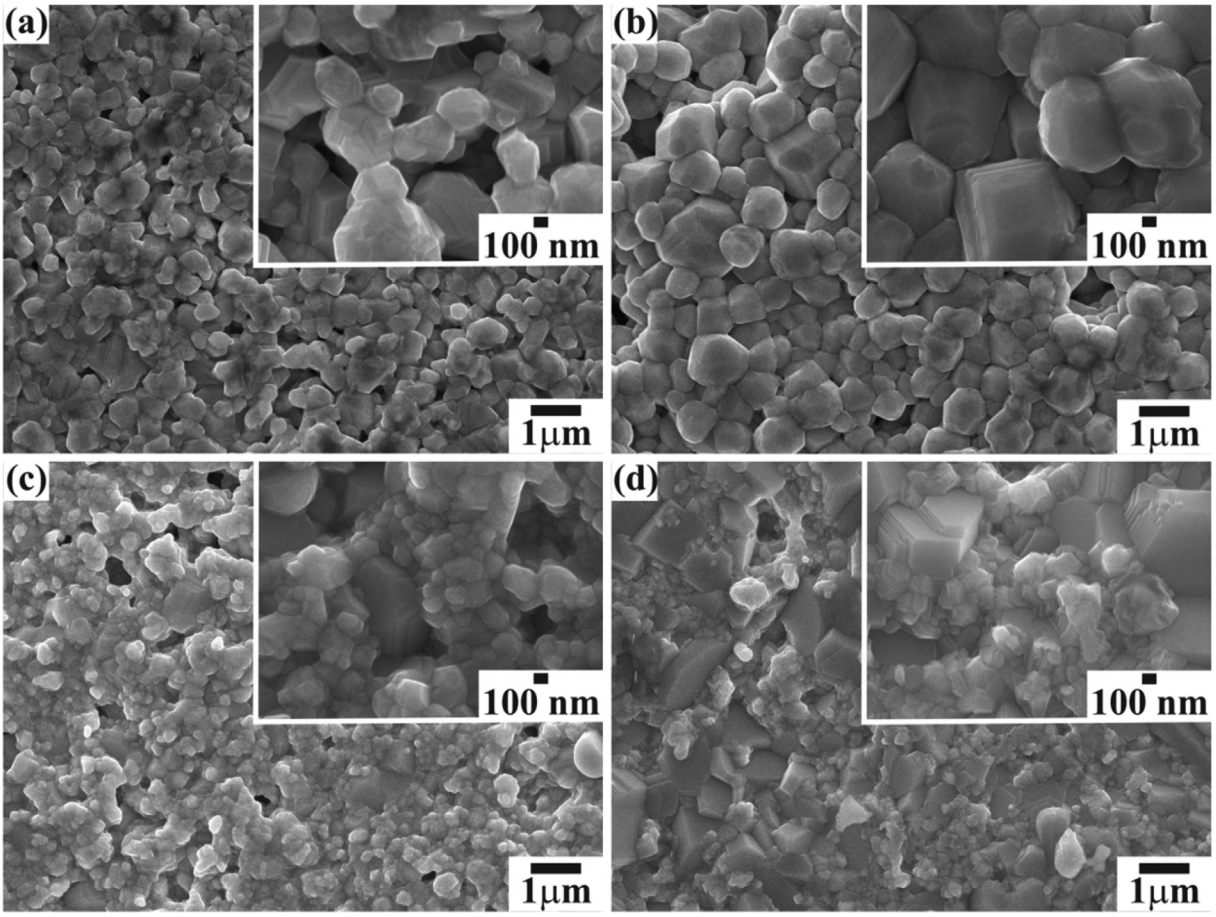

Fig. 3. SEM images of (a) BT, (b) BCT8, (c) Fe(1.25%) doped BCT8, and (d) Fe(5%) doped BCT8. The reduction in size and inhomogeneous distribution with Fe doping is evident (see the magnified view in the inset of these images).

Table 2
Number of bonds and bond length values of Ti–O, Ba–O, Ba–Ti and Ba–Ba bonds obtained from Rietveld analysis of BT, BCT8 and Fe doped BCT8.

Chemical bond	BT		BCT8		BCT8:1.25% Fe		BCT8: 5% Fe	
	No. of bonds	Bond length (Å)	No. of bonds	Bond length (Å)	No. of bonds	Bond length (Å)	No. of bonds	Bond length (Å)
Ti–O	1	1.8758	1	1.8712	1	1.8666	2	1.8939
	4	1.9995	4	1.9948	4	1.9981	2	1.9979
	1	2.1495	1	2.1442	1	2.1390	2	2.1014
Ba–O	4	2.7913	4	2.7847	4	2.7838	1	2.7667
	4	2.8221	4	2.8157	4	2.8203	4	2.7945
	4	2.8771	4	2.8702	4	2.8689	2	2.8230
							4	2.8510
							1	2.8796
Ba–Ti	4	3.4241	4	3.4160	4	3.4173	2	3.4108
	4	3.5083	4	3.4999	4	3.5008	4	3.4567
							2	3.5030
Ba–Ba	4	3.9901	4	3.9808	4	3.9875	4	3.9920
	2	4.0253	2	4.0154	2	4.0056	2	3.9895
							8	5.6438
							2	5.6449
							2	5.6463

levels in the BCT8 sample. The double peak feature of the Ba 3*d*, Ca 2*p*, Ti 2*p*, and O 1*s* are shown in Fig. 4(A–C). The deconvolution of Ba 3d XPS spectrum (Fig. 4(A)) shows a perfect fit to four peaks located at binding energy (BE) values of 777.55, 779.21, 792.87 and 794.51 eV. Among these four peaks, the peaks located at BE~777.55 and 792.87 eV corresponds to the spin-orbit doublet i.e., Ba $3d_{5/2}$ and Ba $3d_{3/2}$, 3*d* core level of Ba ions. The other two represent their respective shoulder peaks. The full width at half maxima (FWHM)

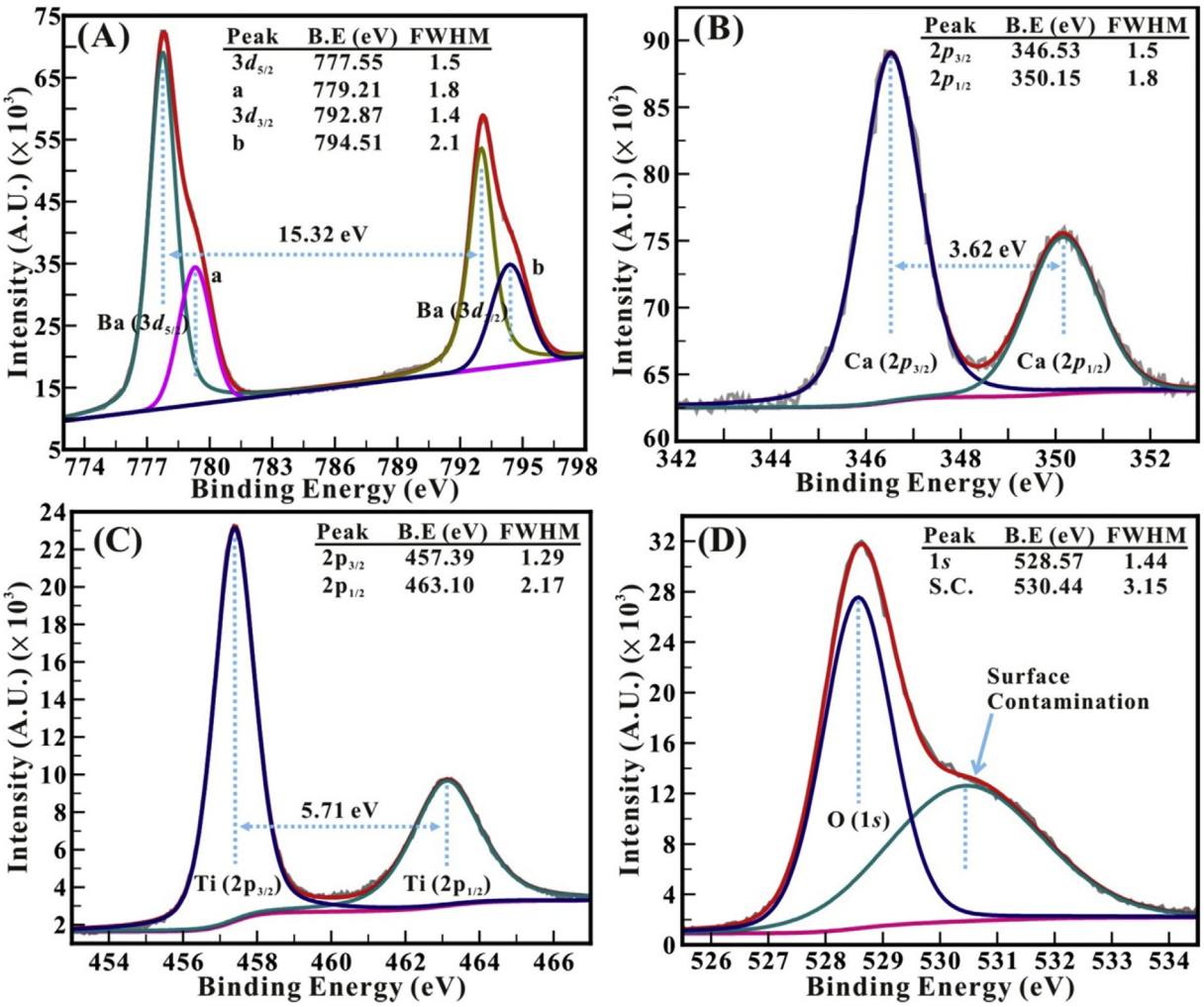

Fig. 4. High resolution XPS data of Ba 3*d* (A), Ca 2*p* (B), Ti 2*p* (C) and O 1*s* (D) peaks in intrinsic BCT8 (without Fe doping). The deconvulted peaks, their respective BE positions and component details are shown inside for each of these core-level peaks.

of the spin-orbit doublet of Ba 3d core level are 1.5 eV and 1.4 eV, respectively. The spin-orbit energy separation (ΔE(Ba 3*d*)) is 15.32 eV between Ba $3d_{5/2}$ and Ba $3d_{3/2}$ core level. These data are comparable to the bulk and nano $BaTiO_3$ [39.40] and confirm the existence of Ba in its characteristic 2+ oxidation state i.e., as Ba^{2+} ions. It should be noted that both the shoulder peaks located at higher BE side are not at all represent the different oxidation state but are present due to the relaxation phase formed at the BCT8 surface in order to reduce surface strain [41].

The deconvoluted Ca 2*p* XPS spectra (Fig. 4(B)) shows perfect fit to two peaks located at BE of 346.53 and 350.15 eV, which corresponds to Ca $2p_{3/2}$ and Ca $2p_{1/2}$ spin-orbit doublet core level of Ca. The FWHMs of these two peaks are 1.5 eV and 1.8 eV, respectively. The spin-orbit energy separation (3.62 eV) and respective energy positions confirm the presence of Ca^{2+} ions [40–42]. No extra peak is observed in these spectra confirm that Ca^{2+} is incorporated in Ba^{2+} of $BaTiO_3$ lattice without any impurity or additional phase formation. The deconvolution of Ti 2*p* XPS spectrum (Fig. 4(C)) also indicates a perfect fit for two peaks located at a BE of 457.39 and 463.10 eV. These two peaks correspond to Ti $2p_{3/2}$ and Ti $2p_{1/2}$ doublet. FWHM of these peaks are 1.29 EV and 2.17 eV, respectively. The spin-orbit energy separation (5.71 eV), respective BE position of the Ti 2*p* doublet and their FWHM are in excellent agreement with the literature [39–44] and supports the existence of Ti^{4+} cations in BCT8. Similarly, the decomposition of O 1*s* XPS spectra of BCT8 (Fig. 4(D)) fits well to two peaks located at BE~ 528.57 and 530.44 eV with FWHMs of 1.44 and 3.15 eV, respectively. The peak located at lower binding energy corresponds to the O 1*s* core level, which is an indicative of oxygen bonded in BCT8. The higher binding energy peak at 530.44 eV is ascribed to the surface contamination such as carbon oxides or hydroxides [44–47]. Overall, the results confirm that the BCT8 samples are composed of only the elements Ba, Ca, Ti and O in its stoichiometric form with no contamination or extra phase formation.

The high-resolution XPS spectra of Ba 3*d* and Ca 2*p* of the Fe-doped BCT8 samples are shown in Fig. 5. Similar to BCT8, the deconvoluted Ba 3*d* XPS spectrum shows double peak features with two respective shoulder peaks (Fig. 5(A and B)). The Ba $3d_{5/2}$ and Ba $3d_{3/2}$ peaks are located at BE~777.43 (±0.12) and 792.75 (±0.12) eV, respectively. The FWHM of these two peaks is 1.5 and 1.5 eV, respectively. The data confirm the presence of Ba^{2+} ions in Fe-doped BCT samples. Furthermore, the shoulder peaks are located at a binding energy of 779.14 (±0.06) and 794.46 (±0.055) eV with a FWHM of 1.9 and 1.9 eV, respectively. These are very similar to that noted in pure BCT8 samples. The energy separation (~15.32 eV) and intensity of the Ba $3d_{5/2}$ and Ba $3d_{3/2}$ peaks remain constant irrespective of the amount of Fe doping into BCT. This confirms that doping of Fe at different concentrations has neither altered the

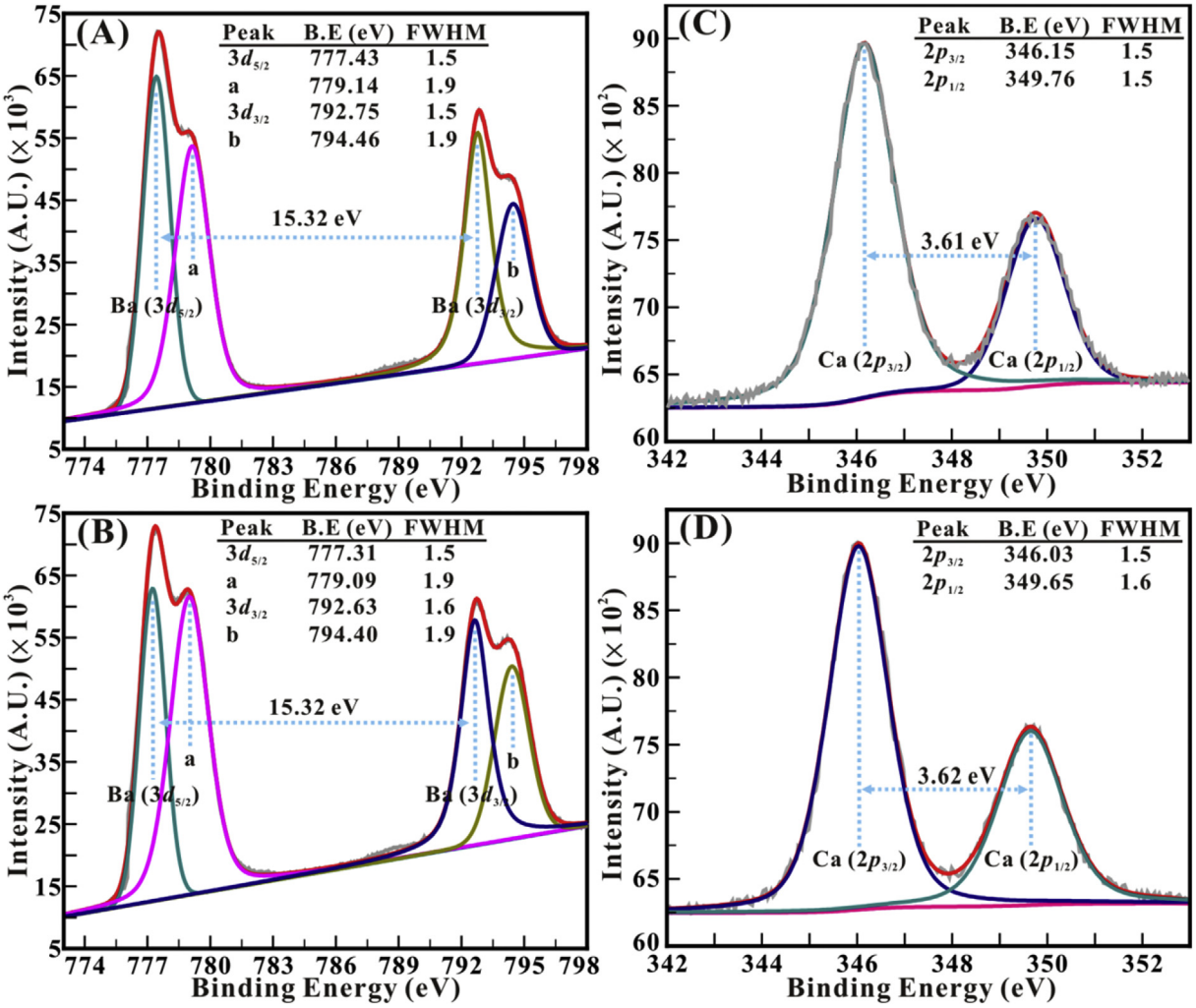

Fig. 5. High resolution XPS data of Ba 3*d* in 1.25% Fe doped BCT8 (A) and 5% Fe doped BCT8 (B) samples. The high resolution XPS data of Ca 2*p* core level in these samples are shown in (C) and (D), respectively. The deconvoluted peaks, their respective BE positions and component details are as indicated inside for each of these core-level peaks.

properties of Ba^{2+} cations nor replaced it from its position. However, the intensity of both the shoulder peaks increased with increasing Fe content. This observation corroborates with the appearance of a high level of strain in the BCT8 with increasing Fe concentration. This could be responsible for the observed decrease in grain size (crystallite size) with Fe doping as observed in FESEM micrographs. Thus, the XPS data confirm that the Ba $3d_{5/2}$ and Ba $3d_{3/2}$ peaks are the general characteristic feature of $BaTiO_3$ only; no evidence is noted for the presence of impurities and/or extra phase formation. Fig. 5(C and D) shows the double peak features of Ca 2*p* for the Fe-doped BCT8 samples. The Ca $2p_{3/2}$ and Ca $2p_{1/2}$ doublet located at BE values of 346.15 (±0.25) and 349.76 (±0.25) eV, respectively, with corresponding FWMH values of 1.5 and 1.5 eV indicate the characteristic of Ca^{2+} cations in the Fe-doped BCT8 sample. It is evident that the intensity of the Ca 2*p* doublet and their spin-orbit energy separation of 3.62 eV remains constant for a variable Fe-doping concentration from 0 to 5%. Thus, the XPS data confirms that there is no significant effect of Fe on either chemical quality or electronic structure of BCT.

The high-resolution XPS spectra of Ti 3*p* and Fe 2*p* core levels are shown in Fig. 6 for the Fe-doped BCT8 samples. The deconvoluted Ti 2*p* (Fig. 6(A and B)) indicates a perfect fit for the two peaks located at the BE of 457.05 (±0.24) and 462.76 (±0.24) eV, respectively. These peaks correspond to the doublet arising from the spin-orbit splitting i.e., Ti $2p_{3/2}$ and Ti $2p_{1/2}$, respectively. The BE location of Ti 2*p* doublet and energy separation of 5.71 eV characterizes the presence of Ti^{4+} cations in the BCT8 sample after Fe doping [35,39,40,44,48]. The deconvoluted XPS spectra of Fe 2*p* region (Fig. 6(C and D)) also shows a perfect fit to two peaks located at a binding energy of 709.76 (±0.08) and 723.08 (±0.06) eV with energy separation of 13.32 (±0.02) eV. These two peaks correspond the doublet, which is due to spin-orbit splitting in Fe 2*p* i.e., Fe $2p_{3/2}$ and Fe $2p_{1/2}$. The BE position of these peaks along with energy separation (ΔE Fe 2*p*) characterizes Fe in its 3+ oxidation state i.e., Fe^{3+} cations [35,36,49,50]. An increase in the intensity of Fe $2p_{3/2}$ and Fe $2p_{1/2}$ observed (Fig. 6(C and D)) with increasing Fe content is an obvious indication of increased Fe concentration in the ceramics with Fe doping. On the other hand, the intensity of Ti $2p_{3/2}$ and Ti $2p_{1/2}$ peaks decrease slightly with increasing Fe concentration from 0 to 5%. This observation reveals that Fe occupies the Ti sites in the Fe-doped BCT8. Overall, the keen observation of XPS spectra indicates that only the Ti $2p_{3/2}$ and Ti $2p_{1/2}$ peak positions are slightly shifted towards the lower BE with increasing Fe content. These Ti peaks located at BE ~457.69 and 463.10 eV experience a negative shift in BE to 457.05 and 462.61 eV, respectively, with increasing Fe doping. This can be attributed to the increase in the number of Fe atoms at the Ti site in the perovskite structure, where binding energy is equally distributed among all atoms and resulted in a

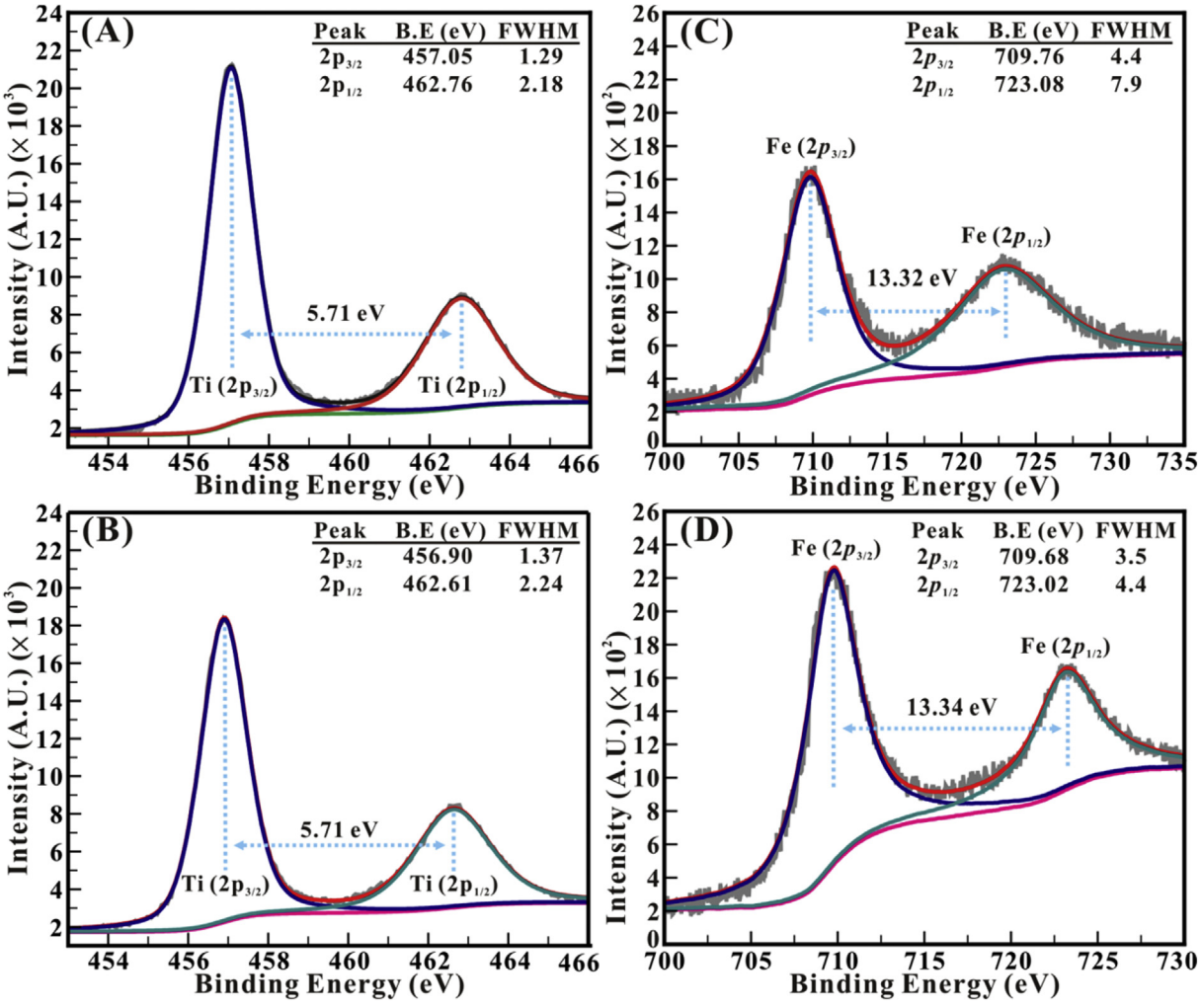

Fig. 6. High resolution XPS data of Ti 2*p* in 1.25% Fe doped BCT8 (A) and 5% Fe doped BCT8 (B) samples. The high resolution XPS data of Fe 2*p* core level in these samples are shown in (C) and (D), respectively. The deconvoluted peaks, their respective BE positions and component details are as indicated inside for each of these core-level peaks.

decrease in the binding energy of Ti (2p) peaks after substitution of Fe at Ti site [51]. Furthermore, while changes in Ti peak with progressive Fe-doping are obviously related to Fe substitution at Ti-site, some changes in the BE or peak shape of the characteristic O *1s* core level are expected if there is any secondary phase segregation, such as Fe-oxides evolving into a separate impurity phase. However, no such changes seen function of Fe doping also confirms the formation of single phase Fe-doped BCT material, where Fe is substituting for Ti. In addition to XRD and XPS analyses, Raman spectroscopic data as discussed below also supports the chemical quality of these ceramics.

Raman spectra measured for all the ceramics at room temperature are shown in Fig. 7. Raman spectroscopic data of these materials can be conveniently used to understand the chemical bonding, chemical quality and phase purity of these materials and the effect of Fe doping. It is well known that there are $3A_1(TO) + 3A_1(LO) + 3E(TO) + 3E(LO) + 1E(TO + LO) + 1B_1$ Raman active modes present in tetragonal ferroelectric phase of $BaTiO_3$ (*P4mm*) whereas these modes are Raman inactive for cubic paraelectric phase of $BaTiO_3$ *(Pm3m)*. In the present case, the observed four distinct Raman peaks viz., $A_1(TO)$, $E(TO + LO)/B_1$, $E(TO)/A_1(TO)$ and $E(LO)/A_1(LO)$ for BT at 260 cm^{-1}, 302 cm^{-1}, 512 cm^{-1} and 712 cm^{-1}, respectively, confirm the tetragonal crystal structure of BT. Similarly for BCT8 ceramics, these phonon peaks were observed approximately at the same position to that of BT. However, decrease in the sharpness of $E(TO + LO)/B_1$ mode can be noted which indicates the slight distortion in the tetragonal structure with Ca substitution.

In case of Fe doped BCT8, along with the decrease in sharpness of $E(TO + LO)/B_1$ mode, the $A_1(TO)$ and $E(TO)/A_1(TO)$ phonon modes become broad and shift slightly towards the lower frequencies which can be explained on the basis of spatial correlation [35]. Also, due to the higher atomic mass of Fe (55.85 g/mol) than that of Ti (47.867 g/mol), the $A_1(TO)$ and $E(TO)/A_1(TO)$ modes shift toward lower frequencies indicating the decrease in average bonding energy of Ti/Fe—O bond since these modes result from the vibration of centered ions of octahedron in ABO_3 perovskite structure. Furthermore, in case of 5% Fe doped BCT8, additional modes around 142 cm^{-1} and 195 cm^{-1} are also present (represented by *). Among these two modes, the mode around 195 cm^{-1} is the characteristic phonon mode of orthorhombic $BaTiO_3$ [52]. The absence of any additional mode in 5% Fe doped BCT8 establish that the 5% Fe doped BCT8 have the pure orthorhombic structure and is in good agreement with the XRD results. It can be concluded from Raman spectroscopic analyses that the Fe (5%) addition in BCT8 transforms the structure from tetragonal to orthorhombic without any trace of impurity phases. Thus, the synthesized Fe doped BCT8 ceramics is a single phase multiferroic material.

The polarization versus electric field (P-E) hysteresis loops for BT, BCT8, and Fe-doped BCT8 are shown in Fig. 8. It is evident that all the samples show typical P-E hysteresis loops which confirm the ferroelectric nature of these samples. The values of the coercive electric field *(E_c)*, remanent polarization *(P_r)* and maximum polarization *(P_{max})* determined for all the samples are tabulated and compared in Table 3. Intrinsic BT and BCT8 (i.e., without Fe doping) exhibit the high values of P_r and P_{max} which may be due to the larger grain size, better crystalline quality, and high *c/a* ratio compared to that of Fe-doped BCT8 samples. However, E_c value increases with increasing Fe concentration in BCT8 ceramics. These observations can be explained based on the structural and morphology characteristics of the respective samples. It should be noted that the grain size, *c/a* ratio, and grain distribution characteristics play an important role in understanding the ferroelectric behavior. It is seen in FESEM that the effect of Fe is significant on the grain growth and morphology of the BCT8 ceramics. Fe-doping induces a non-uniform distribution of grains, as observed from SEM micrographs, along with a random distribution of size and orientation of ferroelectric domains which inhibits the domain wall motion and thus the coercivity increases in Fe-doped BCT due to the pinning of domain walls motion by defect center [28,53].

Strain versus biaxial electric field (S-E) measurements were carried out to better understand the piezoelectric behavior of all these samples. The S-E hysteresis loops obtained for BT, BCT8, and

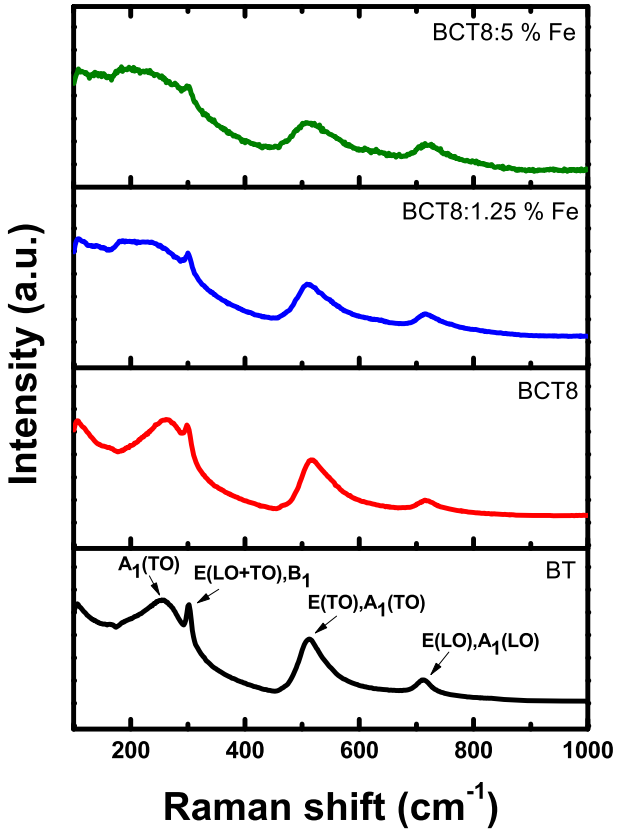

Fig. 7. Raman spectroscopic data of BT, BCT8, Fe(1.25%) doped BCT8, and Fe(5%) doped BCT8 ceramics.

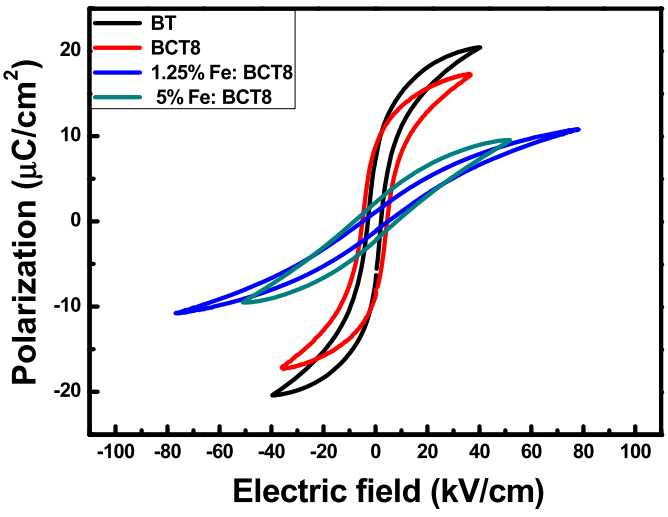

Fig. 8. P-E hysteresis loops of the BT, BCT8, Fe(1.25%) doped BCT8, and Fe(5%) doped BCT8 ceramics.

Table 3
Coercive electric field (E_c), remanent polarization (P_r), maximum polarization (P_{max}), strain %, converse piezoelectric coefficient (d^*_{33}) values of BT, BCT8 and Fe doped BCT8.

Composition	E_c (kV/cm)	P_r (μC/cm^2)	P_{max} (μC/cm^2)	Strain % (pm/V)		d^*_{33} (pC/N)	
				−ve	+ve	−ve	+ve
BT	2.53	6.38	20.43	0.133	0.137	335	339
BCT8	4.34	8.04	17.3	0.093	0.090	258	247
BCT8:1.25%Fe	4.88	0.99	10.8	0.077	0.077	101	98
BCT8:5% Fe	8.15	2.13	9.52	0.037	0.0313	72	62

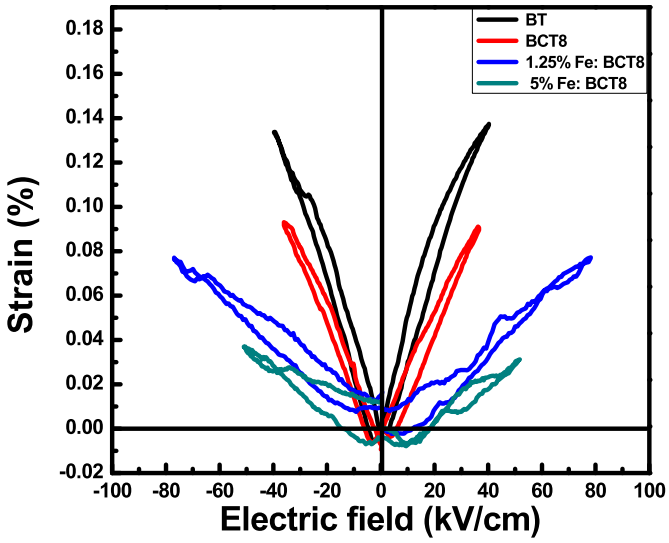

Fig. 9. S-E hysteresis loops of the BT, BCT8, Fe(1.25%) doped BCT8, and Fe(5%) doped BCT8 ceramics.

Fe-doped BCT8 samples are shown in Fig. 9. All the samples exhibit a typical S-E butterfly loop, which confirms the piezoelectric nature of all the samples. From S-E hysteresis loop, the converse piezoelectric coefficient (d^*_{33}) and strain for both the positive and negative electric field are calculated and tabulated in Table 3. Comparison of the S-E hysteresis loops (Fig. 9) indicate that the intrinsic BT and BCT8 samples exhibit symmetric S-E loops while the symmetric nature of S-E loop gradually decreases with Fe doping. This observation indicates that the system is tending to transform from piezoelectric to electrostrictive nature with Fe doping [8] which is also confirmed from XRD. Also, the strain and d^*_{33} decreases with Fe doping. This decrease in strain with Fe doping can be correlated with the grain size. It has been observed from SEM micrographs that, with Fe doping, the grain size decreases and become finer and finer. The grain size reduction decreases the size of domain wall. With decreasing size of domain wall and grain size, it becomes difficult to form the domain walls and thus, it reduces the domain rotation contribution to the strain leading to substantial changes in the hysteresis loop [8,54,55]. Thus, it is concluded that, the degradation of piezoelectric along with the ferroelectric properties occurs with increasing Fe doping in BCT ceramics.

Table 4
Dielectric constant (ε') and dielectric loss (tanδ), Curie temperature (T_c), ε' at T_c for BT, BCT8 and Fe-doped BCT8.

Composition	ε' @ RT	tanδ at RT	(T_c) °C	(ε') @ T_c
BT	935	0.04	120	1691
BCT8	980	0.025	135	4368
BCT8:1.25%Fe	1234	0.020	below RT	1275
BCT8:5% Fe	1835	0.012	below RT	1939

Table 5
Magnetization (M_s) and coercivity (H_c) values of 5% Fe doped BCT8 at 10 K, 100 K and 300 K.

Temperature (K)	(M_s)			(H_c) (Oe)
	emu/g	μ_B/f.u	μ_B/Fe^{3+}	
10	1.837	0.07675	0.01836	380
100	1.58	0.06602	0.01579	179.77
300	1.2175	0.05088	0.01217	13.11

To understand the dielectric behavior of the samples, frequency (50 Hz–1 MHz) dependent dielectric properties of the samples were evaluated. The real part of dielectric constant (ε') and dielectric loss (tan δ) measured at room temperature (RT) are shown in Fig. 10. It is observed that all the samples exhibit the common dielectric dispersion. With increasing frequency from 50 Hz to 1 kHz, there is a rapid decrease of ε'; however, the rate of decrease of ε' is very small with a further increase in frequency from 1 kHz to 10 kHz (Fig. 10(a)). Beyond 10 kHz, ε' becomes almost constant. Beyond certain frequency range, polarization does not follow the frequency of external applied electric field and,

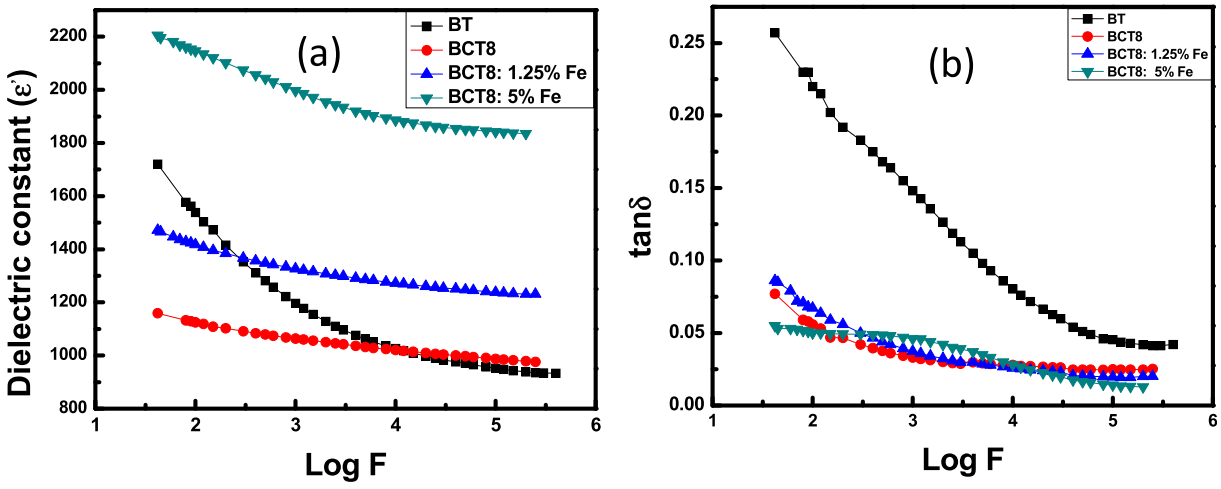

Fig. 10. Variation of (a) dielectric constant and (b) dielectric loss with frequency at RT.

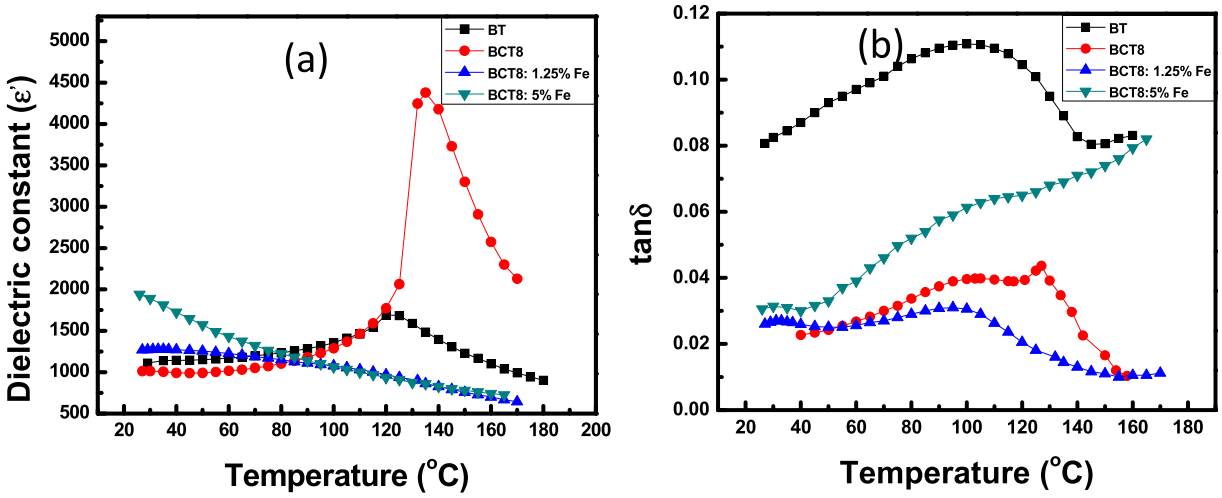

Fig. 11. Variation of (a) dielectric constant and (b) dielectric loss with temperature. Measurements were made at a constant frequency of 10 kHz.

therefore, ε' becomes constant. The higher values of ε' in the lower frequency range (50 Hz-1 kHz) is mainly due to the contribution of different types of polarizations such as ionic polarization, orientational polarization, and space charge/interface polarization. At the higher frequency (>10 kHz), ε' becomes nearly constant. The room temperature variation of tan δ as a function of frequency (Fig. 10(b)) also shows a similar behavior to that of ε' dispersion. The room temperature values of ε' and tan δ at higher frequencies are tabulated in Table 4. It is observed (Table 4) that the 5% Fe-doped BCT8 shows higher value of ε' and lower value of tan δ among all other compositions. This can be attributed to the increased density (Table 1) of BCT8 samples with Fe doping. The lower value of tan δ at a higher frequency (~100 kHz) indicates that the samples can be used for high-frequency data reading/writing in electronic devices (see Table 5).

The temperature (RT-180 °C) dependent ε' and tan δ measured at a constant frequency (10 kHz) for the BT, BCT8 and Fe-doped BCT8 samples are shown in Fig. 11. Intrinsic BT and BCT8 samples (without Fe-doping) show a sharp phase transition from tetragonal (ferroelectric) to cubic (paraelectric) structure around 120 °C and 135 °C, respectively. It is also clearly seen in Fig. 11 (a) and (b) that

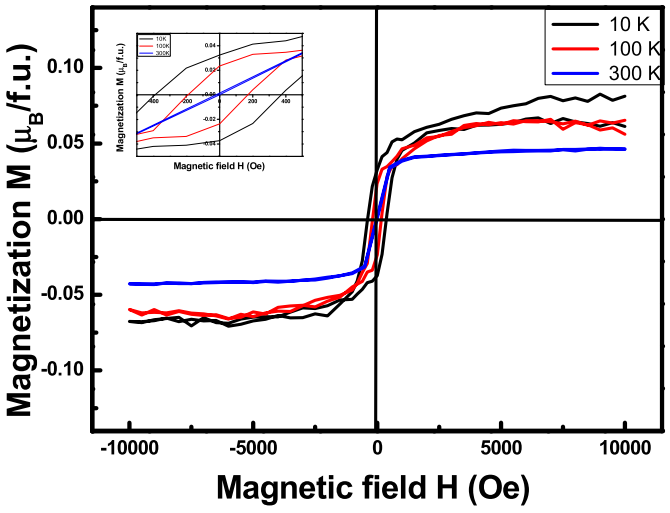

Fig. 12. M-H hysteresis loops for 5% Fe-doped BCT8 at 10 K, 100 K and 300 K.

the ε' at T_c becomes almost double for BCT8 which is in good agreement with the literature and reported data [18]. With Fe doping, Curie temperature (T_c) decreases drastically and reaches close to the room temperature. It is observed (Fig. 11(a)) that, for Fe doped BCT8 samples, the values of T_c are close to the room temperature. At RT, the Fe-doped BCT8 samples indicate the well defined P-E hysteresis loops. The rapid decrease in T_c with Fe doping in BCT8 samples is attributed to the creation of oxygen vacancies due to some of the Fe^{3+} replacing Ti^{4+} as confirmed by XPS analyses. Such oxygen vacancies can lead to the breaking of cooperative vibrations of Ti–O bonds and affect the ferroelectric interactions and dielectric constant [56]. For intrinsic BT and BCT8 (without Fe), the initial increase in ε' with temperature can be explained as follows. It is noted that ε' is nearly temperature independent in the lower temperature range (~ 27 °C–80 °C). This kind of behavior is usually observed if the thermal energy is not enough to increase the mobility of charge carriers. Furthermore, at a higher temperature (above 80 °C), thermal energy increases the mobility of charge carriers and, thus, their hopping rate. The dielectric polarization, therefore, increases rapidly at higher temperature causing ε' to increase up to T_c. At T_c, the hopping rate of charge carriers is maximum. With further increase in temperature beyond T_c, the charge carriers are not able to cope up with the high thermal energy and, as a result, there is a decrease in dielectric polarization, i.e., ε' decreases with further increase in temperature and polarization become random. Therefore, at T_c, the phase transition occurs from the ferroelectric phase to paraelectric phase [57].

The variation of dielectric loss (tan δ) with temperature is shown in Fig. 11(b) for BT, BCT8 and Fe-doped BCT8 samples. It is evident that BT and BCT8 samples show the well-defined single resonance relaxation peak at around 100 °C and 130 °C, respectively. However, Fe-doped BCT8 samples exhibit the two broad yet well-defined resonance relaxation peaks, one at a temperature below 40 °C and other in the temperature range of 80–120 °C. Resonance relaxation peak is observed when the jumping frequency of thermally activated localized electrons become approximately equal to the frequency of the externally applied electric field. At higher temperatures, tan δ increases rapidly and this may be ascribed to the increase in mobility of ions and imperfections in the material i.e., resistivity decreases (conductivity increases) [58]. The BCT samples with highest (5%) Fe concentration shows the higher value of tan δ (as a function of temperature) compared to the other Fe doped samples. This can be attributed to the conductive nature of

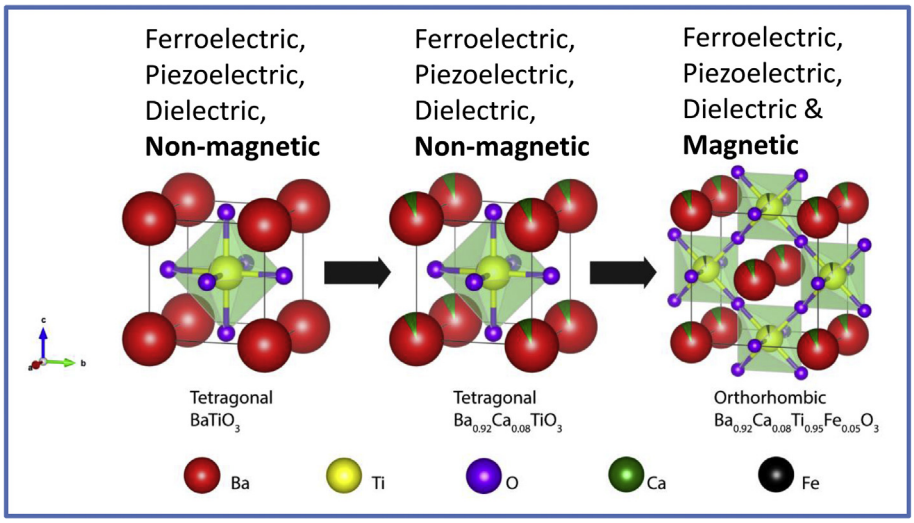

Fig. 13. Proposed schematic model illustrating the structural and property changes as a function of Fe doping into BCT.

the samples with Fe doping, which results in charge transfer, compared to the other samples. The value of tan δ is observed in the range of 0.02–0.07 for the temperature region of 40 °C–140 °C which are lower as compared to BT samples. The lower value of dielectric loss observed for Fe doped BCT8 may be due to the Fe-induced morphology changes [47]. Such changes in dielectric behavior due to changes in the microstructure of ceramics due to doping were also noted in BCT-BZT and other electroceramics [59,60]. Therefore, it can be concluded that the samples synthesized in the present work are of high quality since these samples exhibit low dielectric losses, which is an important requirement for utilizing them in electronic, capacitor and ferroelectric device applications.

Room temperature and low-temperature magnetic measurements (M-H) for all the samples were carried out using vibrating sample magnetometer with maximum applied field of 10 kOe and are as shown in Fig. 12. From the M-H measurements, it is observed that only the 5% Fe-doped BCT8 sample shows magnetic behavior due to the substitution of Fe^{3+} at Ti^{4+} site which can create oxygen vacancies. These oxygen vacancies may act as a kind of medium through which superexchange interactions between neighboring Fe^{3+} ions can occur. The value of saturation magnetization (M_s) and coercivity (H_c) at different temperatures for 5% Fe-doped BCT8 are tabulated in Table 4. The M_s and H_c values are observed to be increasing with a decrease in temperature which is due to the negligible contribution from thermal energy term to magnetization. From the overall observations, it can be considered that the magnetic behavior may arise from the possible defect complexes such as oxygen vacancies and Fe valence fluctuations. Finally, in order to elucidate the correlation between crystal chemistry, chemical composition valence state, ferroelectric, dielectric, piezoelectric, and magnetic properties of the studied ceramics, the conglomeration of the results are presented in Fig. 13. The BT and BCT ceramics are tetragonal and becomes fully orthorhombic for 5% Fe doping into BCT. While intrinsic BT and BCT were exhibiting all other properties, magnetism was fully absent in these materials. Fe-doped BCT8 samples exhibit the magnetic properties in addition to all other characteristics. However, the optimum concentration to obtain such dense, morphology, composition controlled ceramics with the best combination of multiferroic properties is 5% Fe doing into BCT8.

4. Conclusions

Chemical composition controlled intrinsic ($BaTiO_3$, $Ba_{0.02}Ca_{0.08}TiO_3$) and Fe-doped BCT ceramics were synthesized using standard solid state chemical reaction method. Crystal structure analysis confirms that all the BT and BCT8 samples exhibit a single phase, tetragonal structure with space group *P*4*mm*. However, Fe doping induces perturbation to the crystal structure; 5% Fe-doped BCT8 samples exhibit complete structural transformation leading to the orthorhombic structure with space group *Amm*2. The average crystallite size varies in the range of 40–80 nm. Fe-doping induced a reduction in the grain size and increased particle-agglomeration tendency are evident in electron microscopy analyses of the microstructure. XPS analyses provide clues for the origin as well as evidence, in terms of the negative shift in the B.E. for Ti 2*p* doublet along with a decrease in peak intensity, for the doped Fe atoms substituting at Ti site in the BCT crystal structure. Raman spectroscopic data further support and confirms the crystal structure and formation of single phase BT, BCT and Fe-doped BCT materials without any secondary or impurity phases. All of the samples i.e., intrinsic BT, BCT and Fe-doped BCT, exhibit P-E and S-E hysteresis confirming their ferroelectric and piezoelectric nature, respectively. The dielectric constant and dielectric loss follow the usual dielectric dispersion behavior. The Curie temperature (T_c) has been increased from 120 °C for BT to 135 °C for BCT8, while the Fe-doping effect is significant in drastically reducing T_c, which approaches very close to room temperature, due to the Fe^{3+} substitution for Ti^{4+} and, thus, the creation of oxygen vacancies. None of the samples except 5% Fe-doped BCT show evidence for magnetism. Only the 5% Fe-doped BCT8 exhibits magnetic hysteresis at temperatures 300 K, 100 K and 10 K, which may be due to the oxygen vacancies responsible for superexchange interactions between neighboring Fe^{3+}. The optimum composition to obtain ferroelectric and magnetic ordering to be present in a single phase is 5% Fe-doped BCT8. The results, thus, demonstrate that addition of 5% Fe in lead-free BCT8 induces the magnetic ordering and a switchable ferroelectric state, which evidences the presence of multiferroic nature that can be used for four-bit memory and switching applications. The objective of the proposed work to synthesize highly dense, single phase material so that the ferroelectric and magnetic ordering is present in a single phase material is accomplished successfully.

Acknowledgements

Bhavna C. Keswani is thankful to the University Grants Commission (UGC) for the Research fellowship under BSR scheme. Authors at the Pune University are thankful to the Department of Science and Technology, India for financial support (Ref. SR/FTP/PS-040/2010) to carry out the research work. Authors at the University of Texas at El Paso acknowledge with pleasure the support from the National Science Foundation (NSF) with NSF-PREM grant # DMR-1205302.

References

[1] J.F. Scott, Data storage: multiferroic memories, Nat. Mater. 6 (2007) 256–257.
[2] T. Kimura, T. Goto, H. Shintani, K. Ishizaka, T. Arima, Y. Tokura, Magnetic control of ferroelectric polarization, Nature 426 (2003) 55–58.
[3] L. Ju, T. Sabergharesou, K.G. Stamplecoskie, M. Hegde, T. Wang, N.A. Combe, H. Wu, P.V. Radovanovic, Interplay between size, composition, and phase transition of nanocrystalline Cr^{3+} doped $BaTiO_3$ as a path to multiferroism in perovskite-type oxides, J. Am. Chem. Soc. 134 (2012) 1136–1146.
[4] D.Y. Li, Y.J. Zeng, D. Batuk, L.M.C. Pereira, Z.Z. Ye, C. Fleischmann, M. Menghini, S. Nikitenko, J. Hadermann, K. Temst, A. Vantomme, M.J. Van Bael, J.P. Locquet, C. Van Haesendonck, Relaxor ferroelectricity and magnetoelectric coupling in ZnO-Co nanocomposite thin films: beyond multiferroic composites, ACS Appl. Mater. Interfaces 6 (2014) 4737–4742.
[5] M. Bibes, A. Barthélémy, Multiferroics: towards a magnetoelectric memory, Nat. Mater. 7 (2008) 425–426.
[6] Y. Okamoto, Y. Suzuki, Mesoporous $BaTiO_3/TiO_2$ double layer for electron transport in perovskite solar cells, J. Phys. Chem. C 120 (2016) 13995–14000.
[7] N.A. Benedek, C.J. Fennie, Why are there so few perovoskite ferroelectrics? J. Phys. Chem. C 117 (2013) 13339–13349.
[8] N. Setter, ABC of piezoelectricity and piezoelectric materials, in: Piezoelectric Materials in Devices, EPFL, Lausanne, Switzerland, 2002.
[9] K. Uchino, Ferroelectric Devices, Marcel Dekker, 2000.
[10] P.K. Panda, Review: environmental friendly lead-free piezoelectric materials, J. Mater. Sci. 44 (2009) 5049–5062.
[11] C.R. Bowen, H.A. Kim, P.M. Weaver, S. Dunn, Piezoelectric and ferroelectric materials and structures for energy harvesting applications, Energy Environ. Sci. 7 (2014) 25–44.
[12] X. Wang, J. Wu, D. Xiao, J. Zhu, X. Cheng, T. Zheng, B. Zhang, X. Lou, X. Wang, Giant piezoelectricity in potassium–sodium niobate lead-free ceramics, J. Am. Chem. Soc. 136 (2014) 2905–2910.
[13] T.R. Shrout, S.J. Zhang, Lead-free piezoelectric ceramics: alternatives for PZT? J. Electroceram. 19 (2007) 111–124.
[14] C.A. Randall, N. Kim, J.-P. Kucera, W. Cao, T.R. Shrout, Intrinsic and extrinsic size effects in fine-grained morphotropic-phase-boundary lead zirconate titanate ceramics, J. Am. Ceram. Soc. 81 (2005) 677–688.
[15] M.B. Smith, K. Page, T. Siegrist, P.L. Redmond, E.C. Walter, R. Seshadri, L.E. Brus, M.L. Steigerwald, Crystal structure and the paraelectric-to-ferroelectric phase transition of nanoscale $BaTiO_3$, J. Am. Chem. Soc. 130 (2008) 6955–6963.
[16] Hsing-I. Hsiang, Chi-Shiung Hsi, Chun-Chi Huang, Shen-Li Fu, Sintering behavior and dielectric properties of $BaTiO_3$ ceramics with glass addition for internal capacitor of LTCC, J. Alloys. Compd. 459 (2008) 307–310.
[17] Frank Maldonado, Arvids Stashans, DFT study of Ag and La codoped $BaTiO_3$, J. Phys. Chem. Solids 102 (2017) 136–141.
[18] Z. Zhou, C.C. Bowland, B.A. Patterson, M.H. Malakooti, H.A. Sodano, Conformal $BaTiO_3$ films with high piezoelectric coupling through an optimized hydrothermal synthesis, ACS Appl. Mater. Interfaces 8 (2016) 21446–21453.
[19] G.H. Haertling, Ferroelectric ceramics: history and technology, J. Am. Ceram. Soc. 82 (1999) 797–818.
[20] M.M. Vijatović, J.D. Bobić, B.D. Stojanović, History and challenges of barium titanate: part I, Sci. Sinter. 40 (2008) 155–165.
[21] X. Wang, H. Yamada, C.-N. Xu, Large electrostriction near the solubility limit in $BaTiO_3$–$CaTiO_3$ ceramics, Appl. Phys. Lett. 86 (2005), 22905(1-3).
[22] I. Levin, V. Krayzman, J.C. Woicik, Local-structure origins of the sustained curie temperature in (Ba,Ca)TiO_3 ferroelectrics, Appl. Phys. Lett. 102 (2013), 162906 (1-5).
[23] M.T. Buscaglia, V. Buscaglia, M. Viviani, P. Nanni, M. Hanuskova, Influence of foreign ions on the crystal structure of $BaTiO_3$, J. Eur. Ceram. Soc. 20 (2000) 1997–2007.
[24] A. Ianculescu, F.P. Gheorghiu, P. Postolache, O. Oprea, L. Mitoseriu, The role of doping on the structural and functional properties of $BiFe_{1-x}Mn_xO_3$ magnetoelectric ceramics, J. Alloys Comp. 504 (2010) 420–426.
[25] X. Xue, G. Tan, Effect of bivalent CO ion doping on electric properties of $Bi_{0.85}Nd_{0.15}FeO_3$ thin film, J. Alloys Comp. 575 (2013) 90–95.
[26] J.Y. Son, J.-H. Lee, S. Song, Y.-H. Shin, H.M. Jang, Four-states multiferroic memory embodied using Mn-doped $BaTiO_3$ nanorods, ACS Nano 7 (2013) 5522–5529.
[27] M. Valant, I. Arčon, I. Mikulska, D. Lisjak, Cation order–disorder transition in Fe-doped 6H-$BaTiO_3$ for dilute room-temperature ferromagnetism, Chem. Mater. 25 (2013) 3544–3550.
[28] H. Nakayama, H. Katayama-Yoshida, Theoretical prediction of magnetic properties of $Ba(Ti_{1-x}M_x)O_3$ (M = Sc, V, Cr, Mn, Fe, Co, Ni, Cu), Jpn. J. Appl. Phys. 40 (2001) L1355–L1358.
[29] J. Shah, R.K. Kotnala, Induced magnetism and magnetoelectric coupling in ferroelectric $BaTiO_3$ by Cr-doping synthesized by a facile chemical route, J. Mater. Chem. A 1 (2013) 8601–8607.
[30] S.K. Das, R.N. Mishra, B.K. Roul, Magnetic and ferroelectric properties of Ni doped $BaTiO_3$, Solid State Comm. 191 (2014) 19–24.
[31] F. Lin, D. Jiang, X. Ma, W. Shi, Influence of doping concentration on room temperature ferromagnetism for Fe Doped $BaTiO_3$ ceramics, J. Mag. Mag. Mater. 320 (2016) 691–694.
[32] S. Upadhyay, J. Shrivastava, A. Solanki, S. Choudhary, V. Sharma, P. Kumar, N. Singh, V.R. Satsangi, R. Shrivastav, U.V. Waghmare, S. Dass, Enhanced photoelectrochemical response of $BaTiO_3$ with Fe doping: experiments and first-principles analysis, J. Phys. Chem. C 115 (2011) 4373–24380.
[33] C.O. Amorim, F. Figueiras, J.S. Amaral, P.M. Vaghefi, P.B. Tavares, M.R. Correia, A. Baghizadeh, E. Alves, J. Rocha, V.S. Amaral, Magnetoelectric coupling in $BaTiO_3$:$Fe_{113\ ppm}$ nanoscopic segregations, ACS Appl. Mater. Interfaces 7 (2015) 24741–24747.
[34] R. Maier, J.L. Cohn, Ferroelectric and ferrimagnetic iron-doped thin-film $BaTiO_3$: influence of iron on physical properties, J. Appl. Phys. 92 (2002) 5429–5436.
[35] N.V. Dang, T.D. Thanh, L.V. Hong, V.D. Lam, T.-L. Phan, The-long. structural, optical and magnetic properties of polycrystalline $BaTi_{1-x}Fe_xO_3$ ceramics, J. Appl. Phys. 110 (2011), 043914(1-7).
[36] E. Venkata Ramana, S.M. Yang, R. Jung, M.H. Jung, B.W. Lee, C.U. Jung, Ferroelectric and magnetic properties of Fe-Doped $BaTiO_3$ thin films grown by the pulsed laser deposition, J. Appl. Phys. 113 (2013), 187219(1-5).
[37] N. Maikhuri, A.K. Panwar, A.K. Jha, Investigation of A- and B-site Fe substituted $BaTiO_3$ ceramics, J. Appl. Phys. 113 (2013), 17D915(1–3).
[38] V.D. Araújo, F.V. Motta, A.P.A. Marques, C.A. Paskocimas, M.R.D. Bomio, E. Longo, J.A. Varela, Effect of calcium on the structural properties of $Ba_{(1-x)}Ca_xTiO_3$ particles synthesized by complex polymerization method, J. Mater. Sci. 49 (2014) 2875–2878.
[39] C.-X. Li, B. Yang, S.-T. Zhang, D.-Q. Liu, R. Zhang, Y. Sun, W.-W. Cao, Effects of Mn doping on multiferroic and magnetocapacitive properties of $0.33Ba_{0.70}Ca_{0.30}TiO_3$–$0.67BiFeO_3$ diphasic ceramics, J. Alloys Compd. 590 (2014) 346–354.
[40] M. Murata, K. Wakino, S. Ikeda, X-ray photoelectron spectroscopic study of perovskite titanates and related compounds: an example of the effect of polarization on chemical shifts, J. Electron Spectrosc. Relat. Phenom. 6 (1975) 459–464.
[41] M.D. Toomey, K. Gao, G.P. Mendis, E.B. Slamovich, J.A. Howarter, Hydrothermal synthesis and processing of barium titanate nanoparticles embedded in polymer films, ACS Appl. Mater. Interfaces 7 (2015) 28640–28646.
[42] M. del C.B. López, G. Fourlaris, B. Rand, F.L. Riley, Characterization of barium titanate powders: barium carbonate identification, J. Am. Ceram. Soc. 82 (1999) 1777–1786.
[43] H. Zou, D. Peng, G. Wu, X. Wang, D. Bao, J. Li, Y. Li, X. Yao, Polarization-induced enhancement of photoluminescence in Pr^{3+} doped ferroelectric diphase $BaTiO_3$-$CaTiO_3$ ceramics, J. Appl. Phys. 114 (2013) 73103.
[44] J.F. Moulder, W.F. Stickle, P.E. Sobol, K.D. Bomben, Handbook of X-ray Photoelectron Spectroscopy, vol. 8, Physical Electronics, Eden Prairie, MN, 1995.
[45] V. Batra, C.V. Ramana, S. Kotru, Annealing induced changes in chemical bonding and surface characteristics of chemical solution deposited $Pb_{0.95}La_{0.05}Zr_{0.54}Ti_{0.46}O_3$ thin films, Appl. Surf. Sci. 379 (2016) 191–198.
[46] R.S. Devan, C.-L. Lin, S.-Y. Gao, C.-L. Cheng, Y. Liou, Y.-R. Ma, Enhancement of green-light photoluminescence of Ta_2O_5 nanoblock stacks, Phys. Chem. Chem. Phys. 13 (2011) 13441.
[47] R.S. Devan, J.-H. Lin, W.-D. Ho, S.Y. Wu, Y. Liou, Y.-R. Ma, Investigation of high-temperature phase transformation in one-dimensional Ta_2O_5 nanorods, J. Appl. Crystallogr. 43 (2010) 1062–1067.
[48] R.A. Patil, C.-P. Chang, R.S. Devan, Y. Liou, Y.-R. Ma, Impact of nanosize on supercapacitance: study of 1D nanorods and 2D thin-films of nickel oxide, ACS Appl. Mater. Interfaces 8 (2016) 9872–9880.
[49] M. Vargas, D.M. Lopez, N.R. Murphy, J.T. Grant, C.V. Ramana, Effect of W-Ti target composition on the surface chemistry and electronic structure of WO_3-TiO_2 films made by reactive sputtering, Appl. Surf. Sci. 353 (2015) 728–734.
[50] X. Xie, C. Hu, D. Guo, H. Hua, T. Liu, P. Jiang, Room temperature magnetic properties of Fe/Co-doped barium niobate crystals, J. Phys. Chem. C 116 (2012) 23041–23046.
[51] C.V. Ramana, A. Ait-Salah, S. Utsunomiya, J.F. Morhange, A. Mauger, F. Gendron, C.M. Julien, Spectroscopic and chemical imaging analysis of lithium iron triphosphate, J. Phys. Chem. C 111 (2007) 1049–1054.
[52] C.H. Perry, D.B. Hall, Temperature dependence of the Raman spectrum of $BaTiO_3$, Phys. Rev. Lett. 15 (1965) 700–702.
[53] M.C. Chang, S. Sugihara, The electronic states of $Ba_{1-x}Ca_xTiO_3$ and $BaTi_{1-y}Ca_yO_3$ crystalline ceramics, J. Mater. Sci. Lett. 20 (2001) 237–239.
[54] S. Panteny, C.R. Bowen, R. Stevens, Characterization of barium titanate-silver composites part II: electrical properties, J. Mater. Sci. 41 (2006) 3837–3843.
[55] S. Mahajan, O.P. Thakur, C. Prakash, K. Sreenivas, Effect of Zr on dielectric, ferroelectric and impedance properties of $BaTiO_3$ ceramic, Bull. Mater. Sci. 34 (2011) 1483–1489.
[56] P. Kumar, S. Sharma, O.P. Thakur, C. Prakash, T.C. Goel, Dielectric, piezoelectric and pyroelectric properties of PMN-PT (68:32) system, Ceram. Int. 30 (2004) 585–589.

[57] B. Deka, S. Ravi, A. Perumal, D. Pamu, Ferromagnetism and ferroelectricity in Fe doped $BaTiO_3$, J. Phys. B Cond. Matter 448 (2014) 204–206.
[58] I. Coondoo, N. Panwar, H. Amorín, M. Alguero, A.L. Kholkin, Synthesis and characterization of lead-free $0.5Ba(Zr_{0.2}Ti_{0.8})O_3$-$0.5(Ba_{0.7}Ca_{0.3})TiO_3$ ceramic, J. Appl. Phys. 113 (2013) 214107.
[59] P. Mishra, Sonia, P. Kumar, Effect of sintering temperature on dielectric, piezoelectric and ferroelectric properties of BZT–BCT 50/50 ceramics, J. Alloys Compd. 545 (2012) 210–215.
[60] S.G. Kakade, Y.-R. Ma, R.S. Devan, Y.D. Kolekar, C.V. Ramana, Dielectric, complex impedance and electrical transport properties of erbium (Er_{3+}) ion substituted nanocrystalline, cobalt-rich ferrite ($Co_{1.1}Fe_{1-x}Er_xO_4$), J. Phys. Chem. C 120 (2016) 5682–5693.